Theor Chem Acc (2012) 131:1231
DOI 10.1007/s00214-012-1231-x

REGULAR ARTICLE

Effects of Ti doping at the reduced SnO_2(110) surface with different oxygen vacancies: a first principles study

Hua Jin · Wei Lin · Ying Zhang · Jia Zhu · Yi Li · Yongfan Zhang · Kaining Ding · Xin Huang · Wenkai Chen

Received: 22 December 2011 / Accepted: 2 May 2012 / Published online: 22 May 2012

Abstract A series of Ti-doped SnO_2(110) surfaces with different oxygen vacancies have been investigated by means of first principles DFT calculations combined with a slab model. Three kinds of defective SnO_2(110) surfaces are considered, including the formations of bridging oxygen (O_b) vacancy, in-plane oxygen (O_i) vacancy, and the coexistence of O_b and O_i vacancies. Our results indicate that Ti dopant prefers the fivefold-coordinated Sn site on the top layer for the surface with O_b or O_i vacancy, while the replacement of sublayer Sn atom becomes the most energetically favorable structure if the O_b and O_i vacancies are presented simultaneously. Based on analyzing the band structure of the most stable configuration, the presence of Ti leads to the variation of the band gap state, which is different for three defective SnO_2(110) surfaces. For the surface with O_b or O_i vacancy, the component of the defect state is modified, and the reaction activity of the corresponding surface is enhanced. Hence, the sensing performance of SnO_2 may be improved after introducing Ti dopant. However, for the third kind of reduced surface with the coexistence of O_b and O_i vacancies, the sublayer doping has little influence on the defect state, and only in this case, the Ti doping state partly appears in the band gap of SnO_2(110) surface.

Keywords Tin dioxide · Doping · Defect state · Band structure · Density functional theory

H. Jin · Y. Zhang · J. Zhu · Y. Li · Y. Zhang (✉) · K. Ding · X. Huang (✉) · W. Chen
Department of Chemistry, Fuzhou University, Fuzhou 350108, Fujian, China
e-mail: zhangyf@fzu.edu.cn

X. Huang
e-mail: xhuang@fzu.edu.cn

H. Jin
College of Chemistry and Biology Engineering, Yichun University, Yichun 336000, Jiangxi, China

W. Lin
Department of Chemistry and Biochemistry, University of California, San Diego, La Jolla, CA 92093, USA

Y. Li
State Key Laboratory Breeding Base of Photocatalysis, Research Institute of Photocatalysis, Fuzhou 350002, Fujian, China

Y. Zhang
Fujian Provincial Key Laboratory of Theoretical and Computational Chemistry, Xiamen 361005, China

1 Introduction

Tin dioxide (SnO_2) has been receiving extensive investigations because of its wide applications in solar cells, catalysis, and optically transparent materials [1–3]. In particular, SnO_2 is the most important semiconducting metal oxide as gas sensors for detecting various pollutant gases due to its attractive features include simple fabrication process, rapid response and recovery, and low cost [4–13]. However, there are still some limitations and challenges such as low sensitivity, lack of selectivity, and effect of aging for SnO_2-based gas sensor [11, 14, 15]. To improve the sensing performances of SnO_2, many efforts have been made to modify the structure and chemical reactivity of SnO_2.

As pointed out by Williams and Moseley [16], doping with suitable cations can enhance the sensing performances of the semiconducting oxides since cations change the electronic properties and chemical reactivity of the base

material. A lot of experimental studies have indicated that the surface of SnO_2 can be tailored by addition of different metal species, which provide an efficient way to develop new sensor materials with better sensitivity, selectivity, and shorter response time [17–21]. In general, the addition of metal to tin dioxide has two important influences on the sensing performances. First, by doping with metal atom, the new energy level derived from the dopant atom (namely the doping state) may be formed in the band gap of SnO_2, and then, the electric resistance of the SnO_2 is reduced. Correspondingly, the good sensitivity of SnO_2 may be achieved. Second, it is well known that the preparation of the SnO_2 in vacuum always results in oxygen vacancies on the surface, and the addition of metal dopant may facilitate the formation of vacancies on the SnO_2 surface [22]. Accompany with the increase in the concentration of charge carriers, the defect sites can provide new sites for the detection of gas species, since the low-coordinated Sn atoms near the vacancy sites usually show higher reactivity toward the gas molecules [23, 24]. Consequently, the surface reactivity of SnO_2 surface is enhanced, and the gas response and the selectivity to specific gases are improved.

Among different metal-doped tin dioxide systems, the SnO_2/TiO_2-mixed oxides have attracted considerable theoretical and experimental interest [25–32], since TiO_2 is also a good candidate for gas-sensing applications. In addition, it is also partly due to the fact that in the field of photocatalysis, the SnO_2/TiO_2-mixed oxides have a good activity under UV light and visible light [33, 34]. The results of gas-sensing measurements performed by Radecka et al. [35] have drawn a conclusion that small additions of Ti into SnO_2 lattice increase the density of surface active centers for chemisorption of gas molecule. Recently, Sambrano and co-workers analyzed perfect Sn/TiO_2(110) surfaces and found that doping can modify the chemical, electronic, and optical properties of these oxides surfaces [25]. Our previous theoretical work on the Ti-doped perfect SnO_2(110) surfaces also demonstrated that the structural and electronic properties of SnO_2(110) surface are sensitive to the Ti doping site [29]. For the reduced Ti/SnO_2(110) surface, an early density functional theory (DFT) investigation by Yamaguchi group [26] predicted that the Ti atom occupies preferentially the sixfold-coordinated Sn site at the sublayer. However, this conclusion is obtained by using a three-layer SnO_2 cluster, and only the surface with bridging oxygen vacancies was considered in this study. Therefore, further theoretical studies are necessary to get better understanding of the influences of Ti dopant on the structural and electronic properties of the defective SnO_2 surfaces, which is crucial to reveal the mechanism how the Ti doping modifies the sensing performance of SnO_2.

In this paper, the undoped and Ti-doped SnO_2(110) surfaces with three typical kinds of oxygen vacancies have been investigated by using first principles density functional calculations in conjunction with a slab model. We first determine the most favorable site for Ti substitution and compare the thermodynamic stability of different Ti-doped SnO_2(110) surfaces. Next, the variations of the surface relaxation introduced by the Ti doping are discussed. Finally, the electronic structures of three Ti-doped surfaces are carefully investigated, and we mainly focus on the distributions of the defect states that are relative to the formations of surface oxygen vacancies, as well as the doping states that are associated with the Ti dopant.

2 Models and computational methods

The first principles total energy calculations were carried out based on DFT with Vanderbilt ultrasoft pseudopotentials [36], as implemented in the Vienna ab initio simulation package (VASP) [37–40]. The Perdew–Wang GGA exchange–correlation functional [41] was adopted, and the effects of spin polarization were considered. The kinetic cutoff energy was set to 396 eV. Using the above setting of calculation, the optimized lattice parameters for SnO_2 bulk with rutile structure were $a = 4.821$ Å, $c = 3.229$ Å, $u = 0.306$, which are in good agreement with the experimental values of $a = 4.737$ Å, $c = 3.186$ Å, $u = 0.307$ [42].

The (110) surface is the most stable low-index surface of SnO_2 because it has the lowest density of dangling bonds. In the present work, a supercell consisting of a (2×1) surface unit cell (Fig. 1a) was employed and a five-layer periodic slab (in here, for the perfect surface, each layer contains an O–Sn_2O_2–O unit) was adopted to simulate pristine and Ti-doped SnO_2(110) surfaces. Tests for the convergences of the size of Monkhorst–Pack k-point mesh and the thickness of vacuum region were carried out. The results indicated that when the k-mesh size and the vacuum gap were set to $(3 \times 3 \times 1)$ and 7 Å, a good convergence of the surface energy (1.15 J/m^2) for the perfect surface was achieved. During the structural optimization, the outmost three layers were allowed to relax in all directions and no symmetry restrictions were applied. The atoms on the remaining two layers were fixed to the bulk positions.

Since in the present investigation we focus on those states (including defect state and doping state) within the band gap, this requires a good prediction of the band gap of Ti-doped SnO_2(110) surface. It is well known that due to the insufficient cancellation of the self-interaction correction in the local exchange functional, the pure DFT method usually leads to underestimate the band gap for semiconductors and insulators [43, 44]. To overcome this deficiency, the Becke's

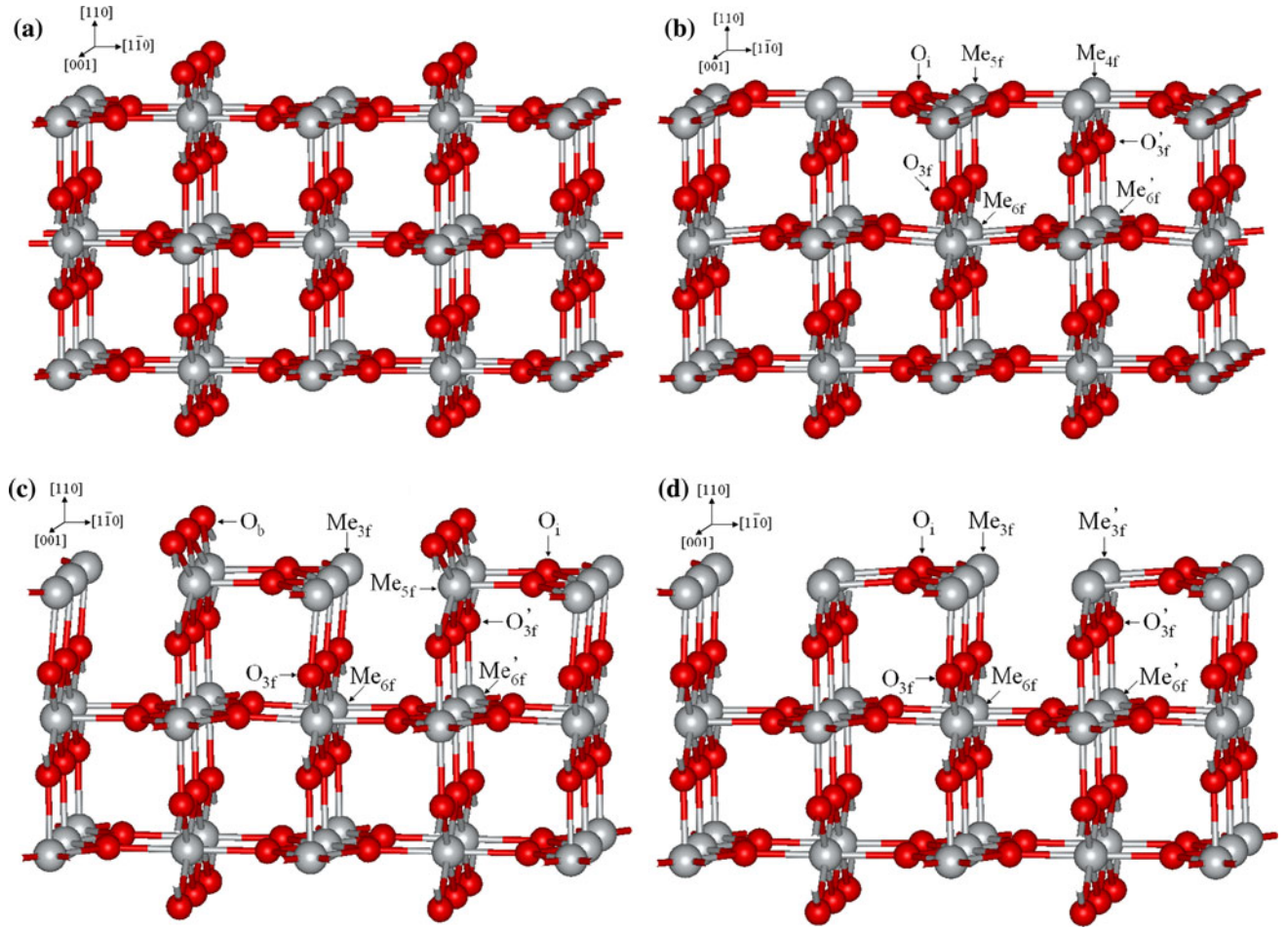

Fig. 1 Schematic side view of (**a**) the perfect $SnO_2(110)$ surface, (**b**) M1 model, (**c**) M2 model, and (**d**) M3 model, respectively. Only the outmost three layers are presented and the symbol of Me denotes metal atoms (Sn or Ti). The *gray* and *red* spheres indicate metal and oxygen atoms, respectively

three-parameter hybrid functional (B3LYP) embedded in the CRYSTAL package [45] was adopted to describe the electronic structure of the systems, and several investigations have shown that this hybrid DFT method can markedly improve the prediction of the band gap of semiconductors and insulators [46, 47]. These further calculations using B3LYP method were based on the linear combination of atomic orbital (LCAO). In this stage, the standard 86-411G basis set constructed by Zicovich-Wilson et al. [48] was employed for Ti atoms, and the basis sets proposed by Calatayud et al. [49] were adopted for the O and Sn atoms, respectively. A (2 × 1) supercell with nine-layer thickness that contains 36 Sn and 72 O atoms (for the perfect surface) was used, and the positions of the atoms at the outmost three layers were derived from the results of above plane-wave calculations. Our previous studies indicated that this two-step procedure could produce reasonable results [29, 50–53].

In this work, three possible configurations of the reduced $SnO_2(110)$ surface were considered, which corresponds to the M1, M2, and M3 models, respectively, as shown in Fig. 1b–d. For the configuration of M1, all the rows of bridging oxygen atoms are removed, leading to the five-fold- and fourfold-coordinated Sn atoms at the top layer (Fig. 1b). In model M2, every other row of in-plane oxygen atoms is lost, and the fivefold- and threefold-coordinated Sn atoms are observed on the surface (Fig. 1c). For the M3 structure, it corresponds to the case of the coexistence of bridging and in-plane oxygen vacancies, in which all bridging oxygen atoms and every second row of in-plane oxygen atoms are removed. As displayed in Fig. 1d, M3 contains two kinds of threefold-coordinated Sn atoms on the surface.

To facilitate the subsequent discussion, we use various symbols to distinguish different metal or oxygen atoms. As shown in Fig. 1, the symbols Me_{4f}, Me_{5f}, and Me_{6f} stand for the fourfold-, fivefold-, and sixfold-coordinated Sn or Ti atoms, respectively. It is noted that for the defective surface, the sixfold-coordinated metal atoms only appear in the sublayers, and symbols Me_{6f} and Me_{6f}' represent two kinds of sixfold-coordinated metal atoms at the second

layer. Similarly, the symbols Me_{3f} and Me_{3f}' are denoted two different threefold-coordinated metal atoms at the top layer in M3 structure (Fig. 1d). Moreover, the symbols O_b and O_i correspond to the bridging oxygen atom and in-plane O atom at the top layer, while two threefold-coordinated O atoms located just below the first-layer metal atoms are labeled as O_{3f} and O_{3f}', respectively.

3 Results and discussion

3.1 Thermodynamic stability of the reduced Ti-doped SnO_2(110) surfaces

As to the (110) surface of the SnO_2 with rutile structure, the Sn ion has two stable oxidation states, namely Sn^{4+} and Sn^{2+}. This alterable valence of Sn implies an easy reduction of the SnO_2(110) surface, and the surface O atoms can be removed or replaced by heating or by particle bombardment [54, 55]. Many experimental and theoretical investigations have been carried out on the reduced SnO_2(110) surfaces [54, 56–60]. Like the rutile-TiO_2(110) surface [61], in the traditional defect model, the reduced SnO_2(110) surface is constructed by removing all the bridging oxygen (O_b) atoms from the stoichiometric bulk termination (see Fig. 1b) [56, 58, 62]. However, Oviedo et al. [56] have carefully studied the stabilities of three types of reduced SnO_2(110) surfaces with removing O_b, subbridging, and in-plane (O_i, see Fig. 1c) oxygen atoms. Their results indicated that at low and intermediate concentrations of vacancy, the surface with O_b vacancy is most stable, while at high concentrations, the configurations of O_b and O_i vacancies show similar thermodynamic stability. According to the experimental results, Batzill et al. [60] have proposed a new model (see Fig. 1d), in which in addition to the removing of O_b atoms, alternating removal of O_i atoms from the adjacent rows also exits in the surface. Accordingly, this structure contains both O_b and O_i vacancies and has a surface layer with a SnO composition. Therefore, in this work, three different reduced SnO_2(110) surfaces, namely M1 $\sim$ M3 models displayed in Fig. 1, are explored.

For each kind of defective SnO_2(110) surface, there are four possible doping configurations that come from the replacements of tin atoms at the top layer and sublayer. For example, in M1 structure (Fig. 1b), the Sn_{5f} and Sn_{4f} atoms at the top layer and the Sn_{6f} and Sn_{6f}' at the sublayer can be substituted by titanium atoms. To study the thermodynamic stability of the reduced SnO_2(110) surface after introducing Ti atom, the doping energy (E_{doping}) for each model is calculated, which is defined as follow,

$$E_{doping} = (E_{Ti-doped} - E_{undoped}) - (\mu_{Ti} - \mu_{Sn}) \quad (1)$$

where $E_{Ti\text{-}doped}$ and $E_{undoped}$ are the total energies of the Ti-doped and undoped reduced SnO_2(110) surfaces, respectively. μ_{Sn} and μ_{Ti} are the chemical potentials of Sn and Ti that are obtained from the corresponding metal bulks, respectively. On the basis of the above definition, the negative value of E_{doping} means that the formation of the Ti-doped reduced SnO_2(110) surface is thermodynamically feasible. The doping energies predicted at the GGA-PW91 level for the Ti-doped SnO_2(110) surfaces with different oxygen vacancies are summarized in Table 1. It is clearly that, from a thermodynamical point of view, the substitution of Ti atom for tin atom on the SnO_2(110) surface is energetically favorable, and the negative values of E_{doping} are obtained for all twelve doping structures. This may be due to the reason that the Ti–O bond is stronger than the Sn–O bond (for instance, in diatomic molecules, the dissociation energies of Ti–O and Sn–O bonds are about 672.4 and 531.8 kJ/mol, respectively [63]). For the M1 and M2 surfaces, the most stable configuration is the replacement of the fivefold-coordinated Sn (Sn_{5f}) atom at the top layer. However, for the M3 surface, the substitution of Ti for a sixfold-coordinated Sn (Sn_{6f}) atom at the sublayer is mostly preferred, and the energy difference between two sublayer doping structures, namely Ti_{6f}- and Ti_{6f}'-doped models, is smaller than 0.1 eV. Overall, it seems that the Ti atoms do not like to replace the low-coordinated Sn atom on the surface, because in such case only few Ti–O bonds are formed. Moreover, the doping energies of sublayer replacements for three different surfaces are similar (about −3.6 eV). In the following sections, we will focus on the structural and electronic properties of those most stable Ti-doped surfaces.

We also study the thermodynamic stability of various structures at different oxygen pressures and temperature conditions, and in here the formation energy, ΔE_{form}, is

Table 1 Calculated doping energies for the Ti-doped SnO_2(110) surfaces with different oxygen vacancies

Structure of the reduced surface	Doping site	Doping energy (eV)
M1 (Fig. 1b)	Sn_{5f}	−3.97
	Sn_{4f}	−3.53
	Sn_{6f}	−3.70
	Sn_{6f}'	−3.47
M2 (Fig. 1c)	Sn_{5f}	−4.05
	Sn_{3f}	−1.62
	Sn_{6f}	−3.54
	Sn_{6f}'	−3.65
M3 (Fig. 1d)	Sn_{3f}	−2.39
	Sn_{3f}'	−2.72
	Sn_{6f}	−3.66
	Sn_{6f}'	−3.57

used as a criterion. For the undoped systems, the quantity of ΔE_{form} refers to the formation energy of $(SnO_x)_n(110)$ surface starting from a SnO_2 bulk and molecular oxygen, namely

$$n\text{SnO}_2(\text{bulk}) + \frac{n(x-2)}{2} O_2 \rightarrow (\text{SnO}_x)_n(110) \tag{2}$$

Thus, ΔE_{form} is defined as

$$\Delta E_{\text{form}} = \frac{1}{n}\left[E^{(\text{SnO}_x)_n(110)} - nE^{\text{SnO}_2(\text{bulk})} - \frac{n(x-2)}{2}E^{O_2}\right] \tag{3}$$

where $E^{(\text{SnO}_x)_n(110)}$, $E^{\text{SnO}_2(\text{bulk})}$, and E^{O_2} are the total energies of a given $(SnO_x)_n(110)$ surface, SnO_2 bulk, and the oxygen molecule, respectively. In addition, n is the number of SnO_x unit in a surface unit cell. While for the defective Ti-doped systems, only the most stable doping structures are considered, and now ΔE_{form} is defined as follows,

$$19n\text{SnO}_2(\text{bulk}) + n\text{TiO}_2(\text{bulk}) + \frac{n(x-40)}{2} O_2 \rightarrow (\text{Ti}/\text{Sn}_{19}\text{O}_x)_n(110) \tag{4}$$

$$\Delta E_{\text{form}} = \frac{1}{n}\left[E^{(\text{Ti}/\text{Sn}_{19}\text{O}_x)_n(110)} - 19nE^{\text{SnO}_2(\text{bulk})} - nE^{\text{TiO}_2(\text{bulk})} - \frac{n(x-40)}{2}E^{\text{O}_2}\right] \tag{5}$$

where $E^{(\text{Ti}/\text{Sn}_{19}\text{O}_x)_n(110)}$ and $E^{\text{TiO}_2(\text{bulk})}$ are the total energies of Ti-doped defective $SnO_2(110)$ surface, TiO_2 bulk in rutile phase, and the coefficient of 19 is related to the number of Sn atom in the surface cell. In addition, to determine the relative stability of different chemical compositions, the free energy change ($\Delta\gamma$) of the above reactions can be obtained from following expressions,

$$\Delta\gamma = \frac{1}{S}[\Delta E_{\text{form}} - n(x-2)\Delta\mu_O(T,p)] \quad \text{(for undoped system)} \tag{6}$$

$$\Delta\gamma = \frac{1}{S}[\Delta E_{\text{form}} - n(x-40)\Delta\mu_O(T,p)] \quad \text{(for Ti} - \text{doped system)} \tag{7}$$

and

$$\Delta\mu_{\text{O}}(T,p) = \mu_{\text{O}} - \frac{1}{2}E^{\text{O}_2} \tag{8}$$

where S is the surface area and μ_{O} is the oxygen chemical potential.

The free energy changes ($\Delta\gamma$·S) for the formation of $(SnO_x)_n(110)$ and $Ti/(SnO_x)_n(110)$ systems as a function of the oxygen chemical potential, $\Delta\mu_{\text{O}}$, are displayed in Fig. 2. For the undoped $SnO_2(110)$ surface, as shown in Fig. 2a, the reduced $SnO_2(110)$ surface only with O_b vacancy is the most favorable structure when $\Delta\mu_{\text{O}} > -1.70$ eV [64], and under reducing conditions, $\Delta\mu_{\text{O}} < -1.70$ eV, M3 is energetically preferred and its surface energy is lower than those of other defective surfaces. Hence, it seems that the reduced $SnO_2(110)$ surfaces with M2 configuration are hardly formed. This conclusion is consistent with the experimental observations of Batzill et al. [60]. With regard to three defective Ti-doped systems (see Fig. 2b), the doping has small influence on the relative stability of three reduced surfaces. The Ti_{5f}-doped M1 model is the most stable structure when the value of $\Delta\mu_{\text{O}}$ is larger than -1.82 eV, while the Ti_{6f}-doped M3 structure becomes energetically favorable at reducing conditions ($\Delta\mu_{\text{O}} < -1.82$ eV). Therefore, our results show that the configuration only with O_i vacancy will be hardly formed in both undoped and Ti-doped $SnO_2(110)$ surfaces and may

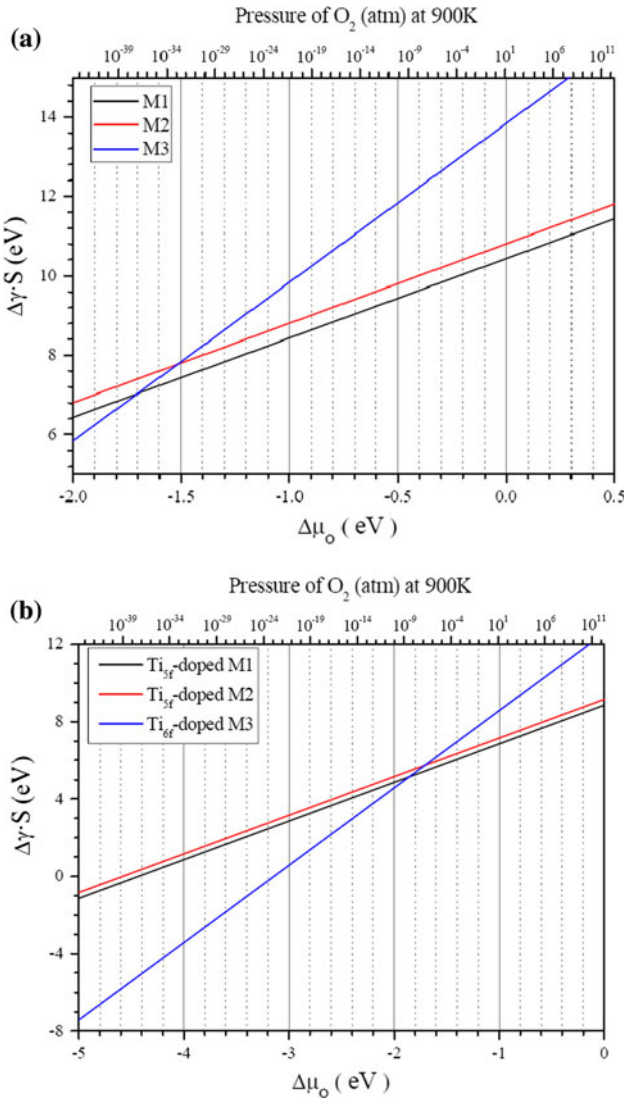

Fig. 2 Free energy change of the formation of (**a**) the undoped and (**b**) Ti-doped defective $SnO_2(110)$ surfaces with different oxygen composition as a function of the oxygen chemical potential $\Delta\mu_{\text{O}}$

be difficult to observe in experiment. Furthermore, according to the curves displayed in Fig. 2, the free energy change for the formation of the reduced $SnO_2(110)$ surface is decreased in the presence of Ti dopant. Compared to the undoped surface, the values of $\Delta\gamma \cdot S$ for M1, M2, and M3 models are decreased about 1.58, 1.65, and 1.27 eV, respectively, which implies that the $SnO_2(110)$ surface can be reduced more easily after introducing the Ti atom.

3.2 Surface relaxations of the reduced Ti-doped $SnO_2(110)$ surfaces

Tables 2, 3, 4 list the displacements of surface atoms along the [110] and [1 $\bar{1}$ 0] directions for the different undoped and Ti-doped reduced surfaces with respect to the ideal $SnO_2(110)$ surface (the relaxations along the [001] direction are small (<0.02 Å) and are not discussed in here). Concerning the undoped defective surfaces, the O_i atom exhibits the largest movement in all models, and it moves toward the vacuum region along [110] direction about 0.195 Å in M1, 0.210 Å in M2, and 0.264 Å in M3 structure, respectively. The obvious displacement of O_i atom is due to the reason that the missing of surface O atom leads to the reducing of the Coulomb interactions between the O_b and O_i atoms, and consequently, the O_i atom tends to move outwards. Similar result is also obtained for the reduced rutile-$TiO_2(110)$ surface, and more significant outward relaxation of O_i (about 0.4 Å) is found in this case [53, 65–67]. According to the data presented in tables, the missing of different kinds of oxygen atoms has various effects on the surface configuration. For the M1 structure, the most obvious relaxations along the [110] direction are found among three undoped models. On the other hand, because of removing one row of in-plane oxygen, remarkable movements along [1 $\bar{1}$ 0] direction are also observed in M2 structure. It is interesting that for the M3 structure, except the outward relaxation of O_i, the displacements of surface atoms are small with respect to the ideal surface, although the O_b and O_i vacancies coexist on this surface.

Since the length of Ti–O bond is usually smaller than that of Sn–O bond, the doping of Ti atom introduces some influences on the configuration of $SnO_2(110)$ surface. As shown in Table 2, when a Ti atom substitutes for a Sn_{5f} atom in the M1 structure, the Ti atom relaxes inward by 0.181 Å; meanwhile compared to the undoped surface, the position of the remaining Sn_{5f} atom changes obviously, which moves toward the vacuum region by about 0.132 Å. In addition, the increase in the outward movement along the [110] direction for the O_i atom is also observed.

For the M2 structure, the most favorable doping of Ti atom also occurs at Sn_{5f} site; however, it must be mentioned that, according to Fig. 1, the fivefold-coordinated Sn_{5f} atoms in M1 and M2 are not the same atom. In this doping model, the relaxation of Ti atom is enhanced, and the magnitudes of displacement along [110] and [1 $\bar{1}$ 0] directions are 0.228 and 0.272 Å, respectively. On the contrary, the relaxation of the remaining Sn_{5f} atom becomes weaken. Due to the short Ti–O bond length, the bridging oxygen atom obviously shifts toward the bulk side

Table 2 Surface displacement (Å) along different directions for the undoped and Ti_{5f}-doped M1 structure with respect to the ideal $SnO_2(110)$ surface

Surface	Undoped M1 structure		Ti_{5f}-doped M1 structure	
Direction	[110]	[1 $\bar{1}$ 0]	[110]	[1 $\bar{1}$ 0]
Me_{5f}[a]	−0.137[b]	0.0	−0.005 (−0.181)[c]	0.007 (0.001)
Me_{4f}	0.192	0.003	0.164	0.003
Me_{6f}	−0.063	0.003	−0.008	0.002
Me_{6f}'	0.094	0.001	0.093	0.001
O_b	–	–	–	–
O_i	0.195	0.086	0.260	0.106
O_{3f}	−0.055	0.009	0.021 (0.034)	0.03 (0.017)
O_{3f}'	0.137	0.016	0.115	0.020

[a] The meaning of each symbol can be found in Fig. 1, and the symbol Me stands for metal atom, namely, Sn or Ti atom

[b] The negative and positive values indicate that the atom moves toward the bulk and vacuum sides, respectively

[c] The values shown in parentheses are corresponding to the results of Ti or its neighboring atom

Table 3 Surface displacement (Å) along different directions for the undoped and Ti_{5f}-doped M2 structure with respect to the ideal $SnO_2(110)$ surface

Surface	Undoped M2 structure		Ti_{5f}-doped M2 structure	
Direction	[110]	[1 $\bar{1}$ 0]	[110]	[1 $\bar{1}$ 0]
Me_{3f}[a]	0.060[b]	0.188	0.049	0.161
Me_{5f}	0.178	0.196	0.035 (0.228)[c]	0.194 (0.272)
Me_{6f}	0.018	0.016	0.015	0.034
Me_{6f}'	0.062	0.010	0.067	0.030
O_b	0.027	0.164	−0.137	0.120
O_i	0.210	0.158	0.186	0.141 (0.073)
O_{3f}	0.029	0.010	0.031	0.017
O_{3f}'	0.093	0.058	0.074	0.076

[a] The meaning of each symbol can be found in Fig. 1, and the symbol Me stands for metal atom, namely Sn or Ti atom

[b] The negative and positive values indicate that the atom moves toward the bulk and vacuum sides, respectively

[c] The values shown in parentheses are corresponding to the results of Ti or its neighboring atom

Table 4 Surface displacement (Å) along different directions for the undoped and Ti_{6f}- and Ti_{6f}'-doped M3 structure with respect to the ideal $SnO_2(110)$ surface

Surface	Undoped M3 structure		Ti_{6f}-doped M3 structure		Ti_{6f}'-doped M3 structure	
Direction	[110]	$[1\bar{1}0]$	[110]	$[1\bar{1}0]$	[110]	$[1\bar{1}0]$
Me_{3f}[a]	0.084	0.064	−0.017	0.044	0.081	0.074
Me_{3f}'	0.119	0.006	0.094	0.014	0.022	0.008
Me_{6f}	0.026	0.019	−0.037 (0.003)	0.015	0.023	0.044 (0.049)
Me_{6f}'	0.053	0.007	0.028	0.008 (0.0)	0.024 (0.029)	0.035
O_b	–	–	–	–	–	–
O_i	0.264	0.036	0.257	0.019	0.267	0.048
O_{3f}	0.041	0.021	−0.060	0.048	0.041	0.046
O_{3f}'	0.078	0.046	0.048	0.050 (0.058)	0.020 (−0.042)	0.039

[a] The meaning of each symbol can be found in Fig. 1, and the symbol Me stands for metal atom, namely, Sn or Ti atom

[b] The negative and positive values indicate that the atom moves toward the bulk and vacuum sides, respectively

[c] The values shown in parentheses are corresponding to the results of Ti or its neighboring atom

by 0.137 Å, and combined with considering the movement of Ti_{5f} atom, the final length of Ti_{5f}–O_b (1.853 Å) bond is shrunk about 0.228 Å with respect to the corresponding Sn_{5f}–O_b (2.081 Å) bond.

The M3 structure is different from above two doping models, and now, the Ti atom prefers to substitute for a Sn_{6f} (or Sn_{6f}') atom at the sublayer. This is a special case that the substitution only introduces a slight change in the surface relaxation (Table 4). Correspondingly, the length of Ti–O bond (about 2.0 Å) in the M3 model is close to that of Sn–O bond, which is larger than the length of Ti–O bond in other top layer doping models. Therefore, it seems that for the M3 model with a SnO surface layer, besides the advantage in thermodynamic stability, the sublayer doping is also expected to benefit from the small deformation of the surface configuration.

3.3 Electronic structures of the reduced Ti-doped $SnO_2(110)$ surfaces

In this section, the band structures (Figs. 3, 4) of the pristine and Ti-doped $SnO_2(110)$ surfaces with different oxygen vacancies are investigated by using the hybrid B3LYP method. In here, we will focus on how the Ti dopant affects the electronic structure of the reduced $SnO_2(110)$ surface, including the variations of the position and component of the defect state, as well as the distribution of the Ti doping state. For the SnO_2 bulk, the band gap obtained by the B3LYP approach is about 3.35 eV, which agrees with the experimental value of 3.6 eV.

Before we discuss the results of the defective surface, it is necessary to make a brief description of the electronic structure of the perfect $SnO_2(110)$ surface. As presented in Fig. 3a, the semiconductor property of SnO_2 bulk is preserved for the perfect surface, and the predicted band gap is about 1.4 eV. By analyzing the components of the energy bands, the valence band maximum is mainly originated from the $2p_y$ state of O_b atom, while the conduction band is dominated by Sn_{5f} 5s orbital in the region between the ***X*** and ***M*** points of the surface Brillouin zone (BZ).

3.3.1 *Electronic structure of the Ti-doped M1 surface*

When all rows of bridging oxygen are removed, namely the M1 model, two new occupied energy bands associated with the defect state appear in the band gap of the perfect surface (Fig. 3b). As a result of the weak localization [59, 68], these bands are strongly dispersed and the calculated bandwidth is about 2.6 eV. Other theoretical works also found that the defect state of $SnO_2(110)$ surface with O_b vacancy extends about 2 eV above the valence band maximum of bulk at the ***M*** point [59, 60, 69]. As labeled in Fig. 3b, the defect state is mainly derived from 5s orbital of the fourfold-coordinated Sn_{4f} atom (denoted by cross), and it also contains some contributions of Sn_{4f} $5p_z$ state (not shown), which can be verified by the corresponding 3D charge density maps displayed in Fig. 5a. It is clear that the charge densities around Sn_{4f} tend to distribute toward the vacuum side due to the hybridization of 5s and $5p_z$ orbitals (namely sp-hybridization). Since the charge densities of the defect state are vertical to the surface and can overlap effectively with the molecular orbitals of the adsorbate, this band gap state may play important roles in the surface reactions, and the Sn_{4f} atom can be seen as an "active" site for the surface reactions. Experimentally, Kawabe et al. have observed the defect state of SnO_2 thin film after Ar ion bombardment at 473 K, and a shoulder peak derived from the rehybridization of Sn 5s and 5p states was

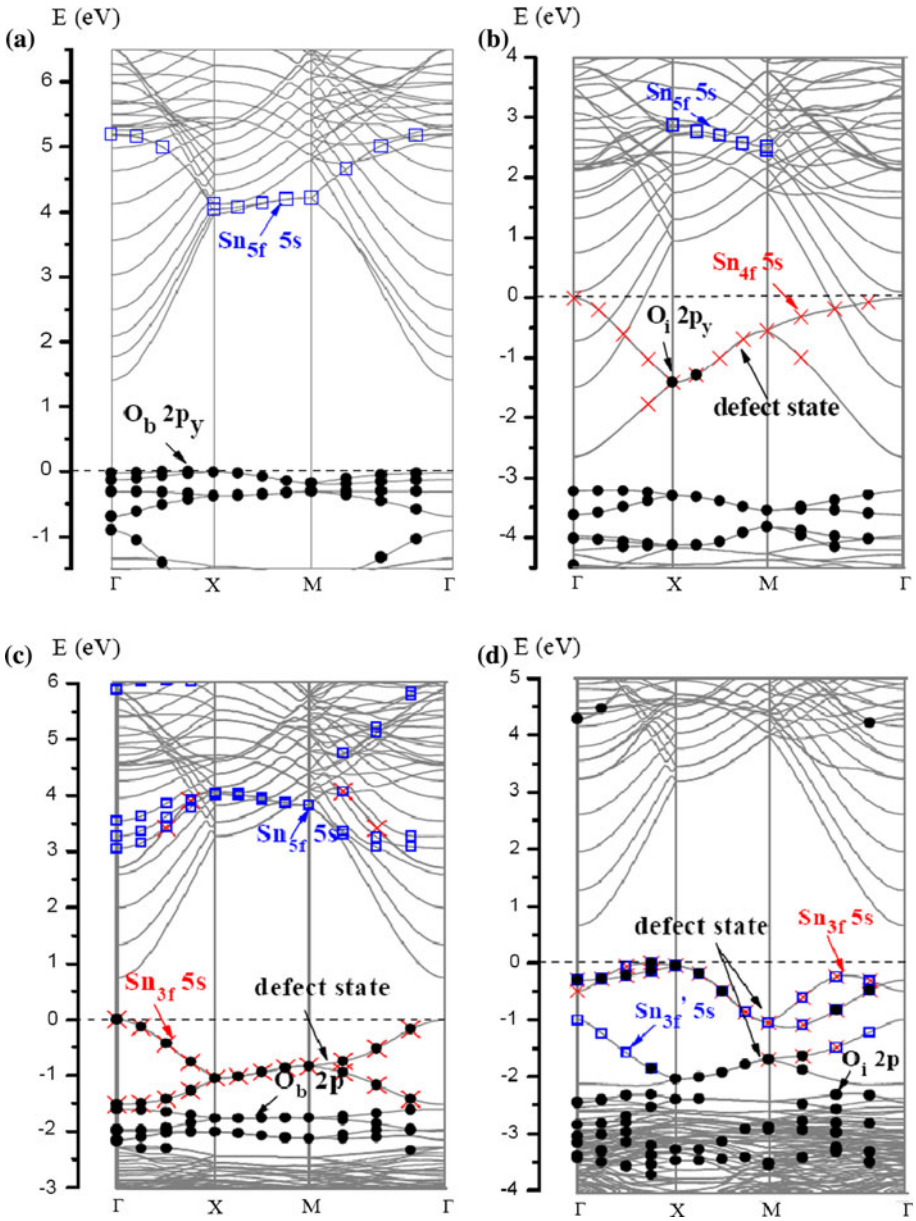

Fig. 3 Band structures of (**a**) stoichiometric $SnO_2(110)$ surface, (**b**) M1 model, (**c**) M2 model, and (**d**) M3 model for the undoped defective $SnO_2(110)$ surfaces. All the energies shown are reported with respect to the Fermi level

determined at the binding energy between 2 and 3 eV [70]. Furthermore, the band gap observed in the perfect surface is disappeared in the M1 model (Fig. 3b), indicating the electric resistance of the SnO_2 is reduced. This enhancement of conductivity is not observed in other reduced surfaces with M2 and M3 structures and can be taken as a representative feature of the $SnO_2(110)$ surface that only contains O_b vacancy.

After introducing Ti atom, for the most stable Ti_{5f}-doped M1 surface, the substitution has some influences on the electronic properties of the surface. First, there are increasing contributions of the O_i 2p states (denoted by filled circle in Fig. 4a) in the defect state, which implies that the covalent interactions between Sn and the neighboring O_i atoms at the top layer are enhanced. Second, it is worth noting that small contributions of Ti_{5f} $3d_{x^2-y^2}$ doping state (denoted by hollow circle) are found in the defect state. Accordingly, the trend of the energy band related to the defect state is changed, especially in the ***X*–*M*** region of BZ. Third, the addition of Ti results in the downward shift of the 5s state of Sn_{5f} atom (denoted by hollow square), and the corresponding energy band partly appears in the band gap around ***M*** point (Fig. 4a). In addition, the substitution of Ti also leads to some Ti 3d energy bands observed in the conduction band of $SnO_2(110)$ surface. The 3D charge density map of the defect state of the Ti_{5f}-doped M1 surface is displayed in Fig. 6a. Since the variation of the composition of the defect state is not obvious, the shape of the 3D charge density map is similar to that of the undoped M1 surface, except that some charge densities located around

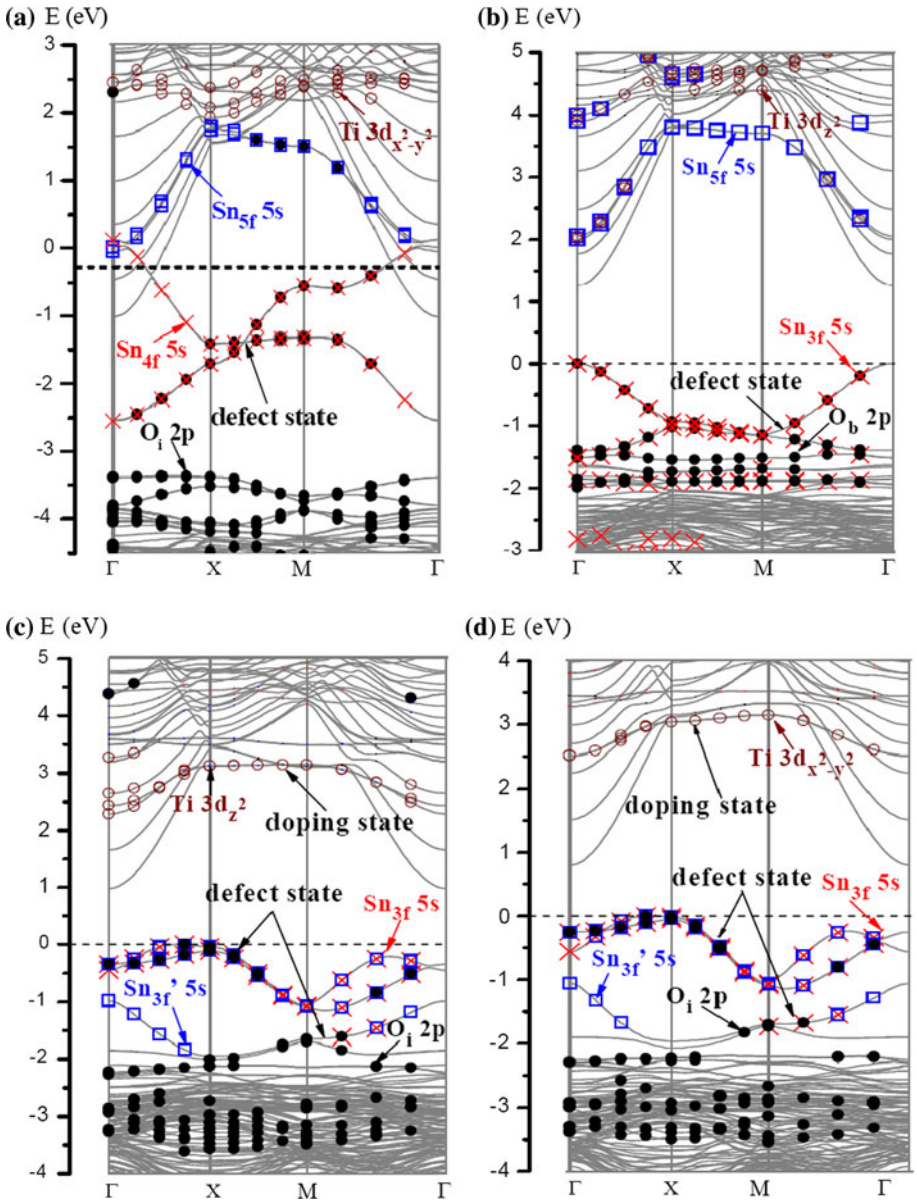

Fig. 4 Band structures of (**a**) Ti_{5f}-doped M1 model, (**b**) Ti_{5f}-doped M2 model, (**c**) Ti_{6f}-doped M3 model, and (**d**) Ti_{6f}'-doped M3 model. All the energies shown are reported with respect to the Fermi level

Ti_{5f} atom are found. Considering the mixing of the contribution of Ti dopant into the defect state and the Ti 3d states appeared in the vicinity of the band gap, Ti_{5f} atoms also become the "active" sites on the surface. Hence, the number of the active center is increased with respect to the undoped surface. So we can expect that, as observed in the experimental work [71], the substitution of Ti for Sn_{5f} atom on the M1 structure could improve the effectiveness of SnO_2 sensor through increasing the density of active centers.

3.3.2 Electronic structure of the Ti-doped M2 surface

For the pristine M2 surface, the main feature of the band structure is that two new occupied energy bands associated with the defect state appear in the band gap of the perfect SnO_2(110) surface (Fig. 3c). Unlike the M1 structure, the SnO_2(110) surface maintains its semiconductor character after losing half of in-plane oxygen atoms, and the value of the band gap is 0.74 eV. In this case the main composition of the defect state is the 2p orbital of the O_b atom, which can be seen clearly in the corresponding 3D charge density map displayed in Fig. 5b. Additionally, it also contains some components of threefold-coordinated Sn_{3f} atoms and the surrounding oxygen atoms (O_i and O_{3f}'). Compared to the M1 structure, the bandwidth of the defect state is reduced about 1.0 eV.

For the most stable doping configuration of M2 structure, the Ti_{5f}-doped M2 surface, introducing Ti at Sn_{5f} site gives rise to the increasing (about 0.52 eV) of the band

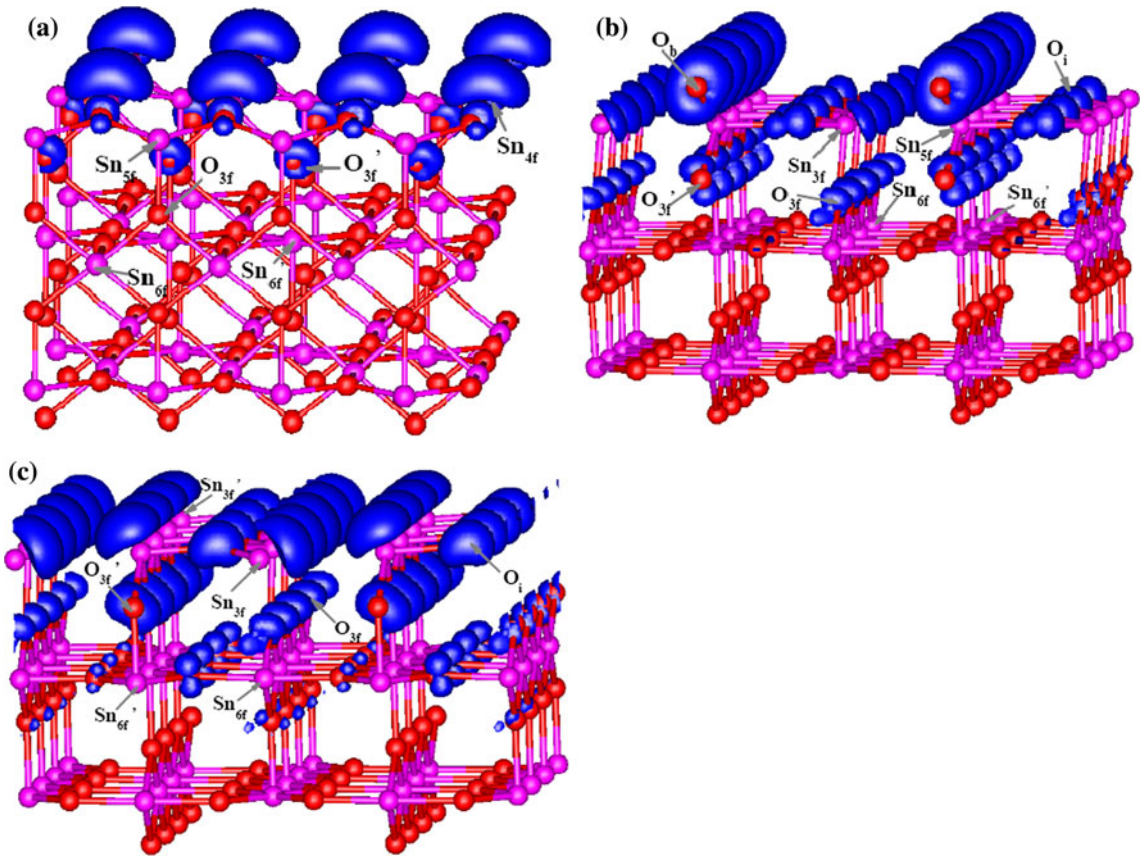

Fig. 5 Side views of 3D charge density maps associated with three pristine defective $SnO_2(110)$ surfaces. In the figures, the Sn and O atoms are denoted by *pink* and *red balls*, respectively. Only the *top* three layers are shown in the pictures

gap. This enlargement of the band gap is directly related to the variation of the surface structure, which results in the upward shift of the conduction band. According to Fig. 4b, the obvious components derived from O_b 2p orbitals are still preserved in the defect state. However, an exception is that the composition of Sn_{3f} 5s becomes more prominent in the defect state, and as demonstrated in Fig. 6b, the charge densities around Sn_{3f} atoms are increased obviously with respect to the case of the undoped surface (Fig. 5b). Therefore, it seems that the activity of the Sn_{3f} atom is enhanced after replacing the Sn_{5f} by Ti atom in the M2 structure. As shown in Fig. 4b, the doping state originated from Ti $3d_z^2$ orbital can be found in the region close to the conduction band, but it is still invisible in the band gap.

3.3.3 Electronic structure of the Ti-doped M3 surface

When all O_b atoms and every second row of O_i atoms are removed simultaneously, for this strongly reduced M3 model with a SnO surface layer, it still exhibits semiconductor character. As shown in Fig. 3d, the minimum band gap of M3 structure (about 0.66 eV) is corresponding to an indirect transition from the valence band at the point near *X* to the conduction band at Γ point. Since there are two kinds of low-coordinated Sn atoms (namely Sn_{3f} and Sn_{3f}', see Fig. 1d) on the surface, more energy bands related to the defect state emerge in the band gap. As presented in Fig. 3d, the energy bands appeared in the band gap are dominated by the 5s orbital of two threefold-coordinated Sn atoms and are also partly made up of the 2p states of neighboring oxygen atoms, which can be confirmed by the 3D charge density map displayed in Fig. 5c.

After a Sn_{6f} (or Sn_{6f}') atom at the sublayer is replaced by Ti atom, the semiconductor property of $SnO_2(110)$ surface is maintained, except that the minimum band gap is increased from 0.66 eV of undoped surface to 0.98 eV of Ti_{6f}- and 0.80 eV of Ti_{6f}'-doped surfaces, respectively. For these cases the addition of Ti dopant inside the bulk has small influence on the energy bands associated with the defect state, and the charge density distributions of the defect state of two sublayer Ti-doped models (Fig. 6c, d) are very similar to the undoped M3 surface. However, a distinct feature of the sublayer doping is that several energy bands dominated by Ti 3d components are presented in the band gap of undoped surface. So the doping state in these systems can be observed, especially in the region between ***X*** and ***M*** points (see Fig. 4c, d). It is noted that the appearance of doping state in the band gap is also achieved

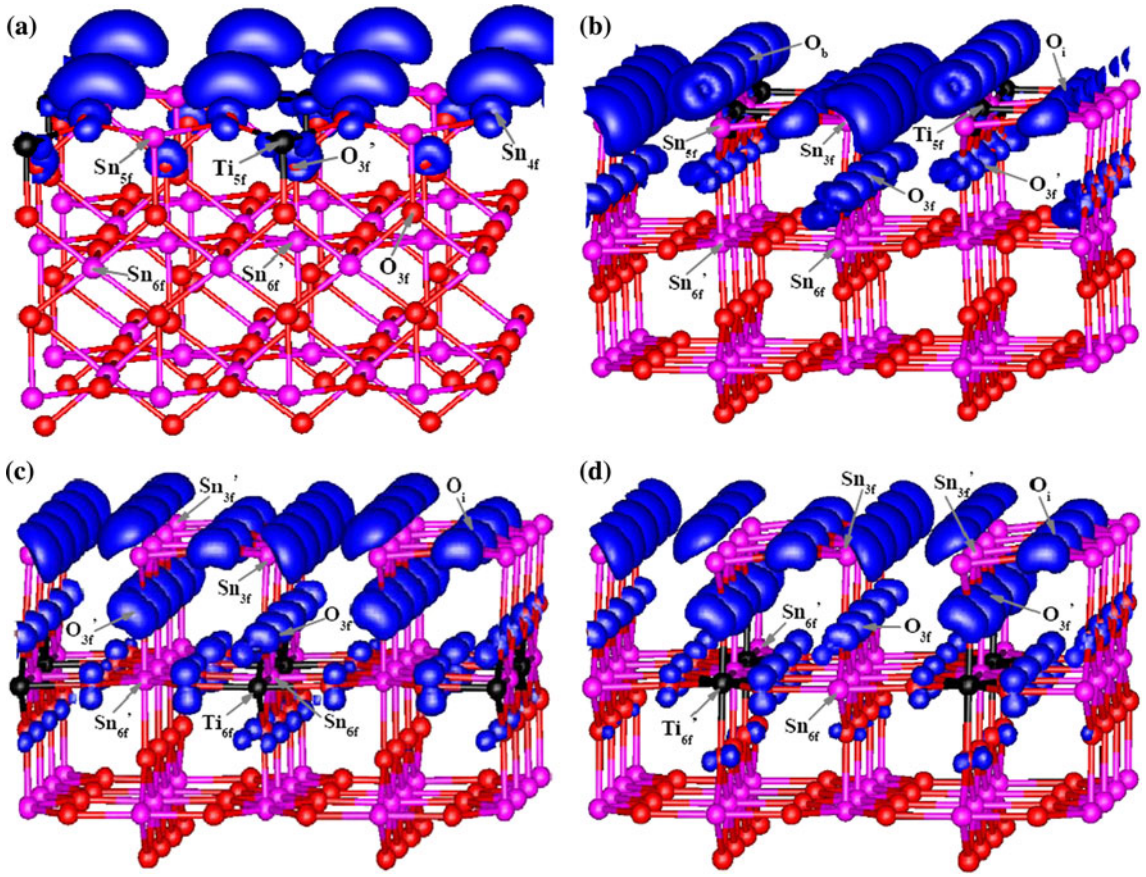

Fig. 6 Side views of 3D charge density maps associated with the defect state of the most stable Ti-doped defective $SnO_2(110)$ surfaces. In the figures, the Ti, Sn and O atoms are denoted by *dark*, *pink* and *red balls*, respectively

for those sublayer Ti-doped M1 and M2 surfaces, as well as for the Ti-doped perfect $SnO_2(110)$ surface [29]. The difference in the distribution of Ti 3d state between the top layer and sublayer substitutions is due to the different strength of the interaction between Ti and O atoms. As discussed in Sect. 3.2, the change in the surface relaxation is small when a sublayer Sn atom is replaced by Ti atom, implying the length of Ti–O bond is close to that of Sn–O bond. In Ti_{6f}- and Ti_{6f}'-doped M3 models, the Ti–O bonds (about 2.0 Å) are longer than those in the top layer-doped surface (about 1.86 Å). Hence, compared with the case of top layer doping, the weaker interaction between Ti and O atoms can be expected for the sublayer-doped model. Consequently, the Ti 3d state tends to shift toward the Fermi level and finally drops into the band gap. We think that this characteristic can be used as a criterion to determine whether the Ti doping site is inside the SnO_2 bulk. From the 3D charge density maps displayed in Fig. 7, the Ti $3d_z^2$ and $3d_{x^2-y^2}$ orbitals are the main components for Ti_{6f}- and Ti_{6f}'-doped M3 models, respectively. Although in these models there is doping state in the band gap, the introducing of Ti has little influence on the reaction activity of $SnO_2(110)$ surface, since the Ti dopant at sublayer cannot directly take part in the surface reaction and as mentioned above, the defect state is not affected obviously by the doping.

4 Conclusions

In this paper the atomic structures and electronic properties of Ti-doped $SnO_2(110)$ surfaces with different oxygen vacancies have been investigated by means of first principles DFT calculations, and a total of 12 configurations of doping models are considered in the present work. Our results show that Ti dopant prefers the Sn_{5f} site on the top layer for the reduced $SnO_2(110)$ surfaces with M1 or M2 configuration, while for the M3 surface with a SnO surface layer, the replacement of sublayer Sn atom becomes the most energetically favorable structure. Moreover, the results of free energy change for the formation of the defective surface indicate that the $SnO_2(110)$ surface can be reduced more easily after introducing the Ti atom. Besides the surface relaxations, the Ti doping has some

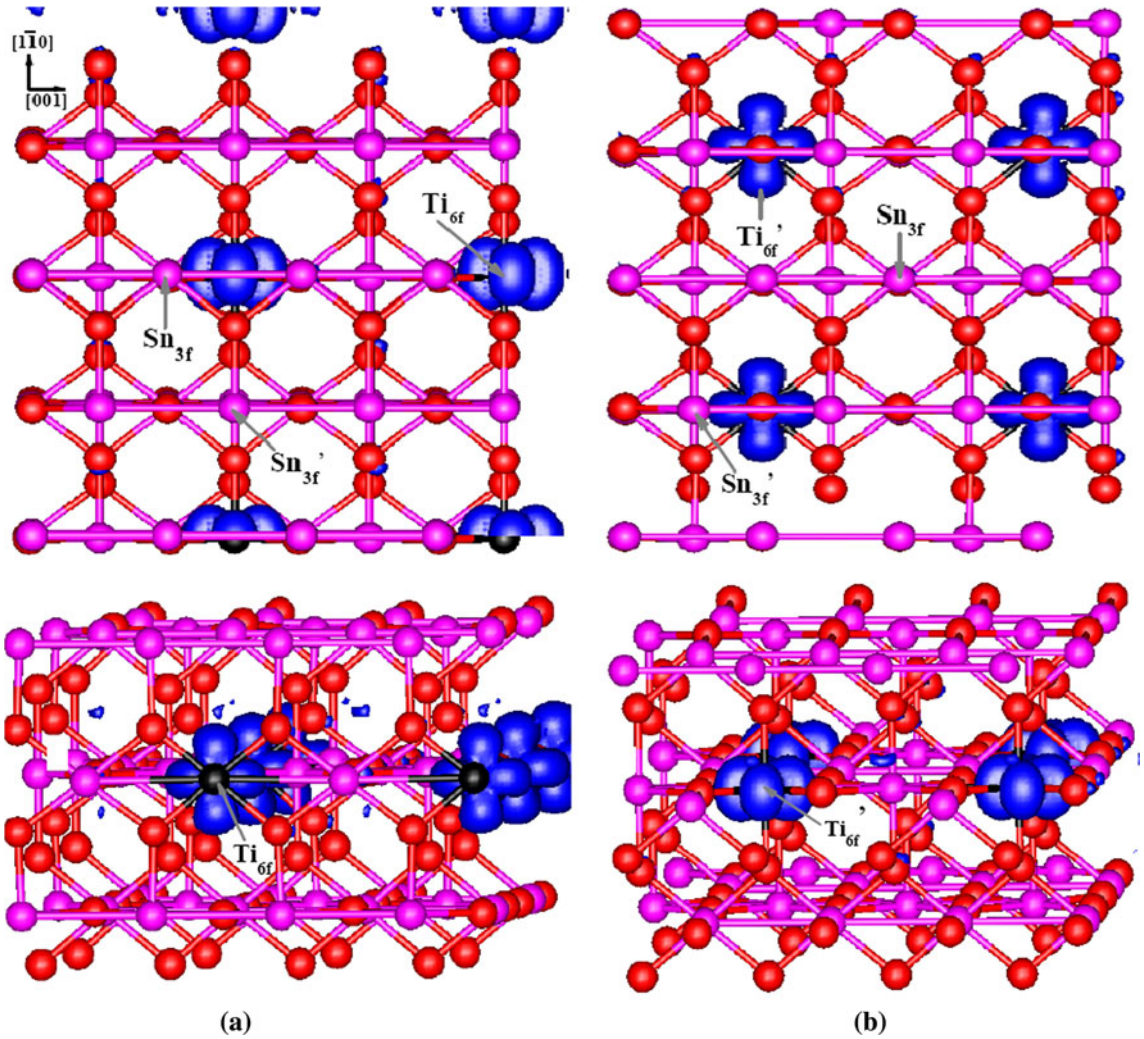

Fig. 7 *Top* and side views of 3D charge density maps associated with the doping state of Ti_{6f}- and Ti_{6f}'-doped M3 models. In the figures, the Ti, Sn and O atoms are denoted by *dark*, *pink* and *red balls*, respectively

influences on the component and position of band gap states of the reduced SnO_2(110) surfaces. However, the detailed effect on the electronic structures of three most stable Ti-doped surfaces is different. For the M1 model, the mixture of Ti 3d component into the defect state is observed, implying that the surface activity is enhanced. The enhancement of the surface activity is also expected for the M2 model, because comparing with the undoped surface, the threefold-coordinated Sn_{3f} atom shows more contribution to the defect state. Therefore, it seems that Ti dopant is an effective additive to improve the sensing performance of SnO_2 surface with M1 or M2 configuration. For the M3 structure, the defect state is almost unchanged by the sublayer substitution, and accordingly, the sensor behavior of M3 model has no obvious change after doping. However, the photocatalysis activity of M3 surface may be modified since the energy bands derived from Ti dopant partly appear in the band gap.

Acknowledgments This work was supported by National Natural Science Foundations of China (grant nos. 21073035, 21071031, 90922022, and 21171039). Y. Z. and W. C. also would like to thank the programs for New Century Excellent Talents in University of Fujian Province (grant nos. HX2006-97, HX2006-103). We are grateful for the generous allocation of computer time on the high-performance computer center of Fujian Province.

References

1. Green ANM, Palomares E, Haque SA, Kroon JM, Durrant JR (2005) J Phy Chem B 109:12525–12533
2. Turrion M, Bisquert J, Salvador P (2003) J Phys Chem B 107:9397–9403
3. Glowacki BA, Yan XY, Fray D, Chen G, Majoros M, Shi Y (2002) Physica C 372:1315–1320
4. Wang CX, Yin LW, Zhang LY, Xiang D, Gao R (2010) Sensors 10:2088–2106
5. Zou XJ, Ding KN, Zhang YF, Yao SS (2011) Theor Chem Acc 128:63–72
6. Habgood M, Harrison N (2008) Surf Sci 602:1072–1079

7. Inerbaev TM, Kawazoe Y, Seal S (2010) J Appl Phys 107:104504-1-7
8. Law M, Kind H, Kim F, Messer B, Yang P (2002) Angew Chem Int Ed 41:2405–2408
9. Maiti A, Rodriguez JA, Law M, Kung P, McKinney JR, Yang P (2003) Nano Lett 3:1025–1028
10. Comini E, Faglia G, Sberveglieri G, Pan Z, Wang ZL (2002) Appl Phys Lett 81:1869–1871
11. Batzill M, Diebold U (2005) Prog Surf Sci 79:47–154
12. Batzill M, Diebold U (2007) Phys Chem Chem Phys 9:2307–2318
13. Batzill M (2006) Sensors 6:1345–1366
14. Cassia-Santos MR, Souas VC, Oliveria MM, Sensato FR, Bacelar WK, Comes JW, Longo E, Leite ER, Varela JA (2005) Mater Chem Phys 90:1–9
15. Itoh T, Matsubara I, Kadosaki M, Sakai Y, Shin W, Izu N, Nishibori M (2010) Sensors 10:6513–6521
16. Williams DE, Moseley PT (1991) J Mater Chem 1:809–814
17. Lavacchi ACB, Rovida G, Bardi U, Atrei A, Angelucci R, Dori L, Nicoletti S (2000) Sens Actuator B 71:123–126
18. Wang Y, Mu Q, Wang G, Zhou Z (2010) Sens Actuators, B 145:847–853
19. Kolmakov A, Klenov DO, Lilach Y, Stemmer S, Moskovits M (2005) Nano Lett 5:667–673
20. Tai W, Oh JH (2002) Sens Actuator B 85:154–157
21. Niranjan RS, Hwang YK, Kim DK, Jhung SH, Chang JS, Mulla IS (2005) Mater Chem Phys 92:384–388
22. Wang Y, Brezesinski T, Antonietti M, Smarsly B (2009) ACS Nano 3:1373–1378
23. Abee MW, Cox DF (2002) Surf Sci 520:65–77
24. Bredow T, Pacchioni G (2005) Theor Chem Acc 114:52–59
25. Sambrano JR, Nobrega GF, Taft CA, Andres J, Beltran A (2005) Surf Sci 580:71–79
26. Yamaguchi Y, Nagasawa Y, Tabata K, Suzuki E (2002) J Phys Chem A 106:411–418
27. Sambrano JR, Vasconcellos LA, Martins JBL, Santos MRC, Longo E, Beltran A (2003) J Mol Struct Theochem 629:307–314
28. Sensato FR, Custodio R, Longo E, Beltrán A, Andrés J (2003) Catal Today 85:145–152
29. Lin W, Zhang YF, Li Y, Ding KN, Li JQ, Xu YJ (2006) J Chem Phys 124:054704-8
30. Yang J, Li D, Wang X, Yang X, Lu L (2002) J Solid State Chem 165:193–198
31. Cao Y, Zhang XT, Yang WS, Du H, Bai YB, Li TJ, Yao JN (2000) Chem Mat 12:3445–3448
32. Zhang ZL, Ma J, Yang XY (2003) J Chem Eng 95:15–52
33. Trotochaud L, Boettcher SW (2011) Chem Mater 23:4920–4930
34. Harunsani MH, Oropeza FE, Palgrave RG, Egdell RG (2010) Chem Mater 22:1551–1558
35. Radecka M, Przewoznik J, Zakrzewska K (2001) Thin Solid Films 391:247–254
36. Vanderbilt D (1990) Phys Rev B 41:892–895
37. Kresse G, Furthmüller J (1996) Phys Rev B 54:11169–11186
38. Kresse G, Hafner J (1993) Phys Rev B 47:558–561
39. Kresse G, Furthmüller J (1996) Comput Mater Sci 6:15–50
40. Kresse G, Hafner J (1994) Phys Rev B 49:14251–14269
41. Perdew JP (1991) In: Ziesche P, Eschrig HE (eds) Electronic structure of solids'91, vol. 1. Berlin, Academie Verlag, (Interscience, New York, 1964)
42. Wyckoff RWG (1968) Crystal structures, vol 4, 2nd edn. Wiley, New York
43. Perdew JP, Levy M (1983) Phys Rev Lett 51:1884–1887
44. Zunger A, Perdew JP, Oliver GL (1980) Solid State Commun 34:933–936
45. Dovesi R, Saunders VR, Roetti C, Orlando R, Zicovich-Wilson CM, Pascale F, Civalleri B, Doll K, Harrison NM, Bush IJ, D'Arco Ph (2009) Llunell M CRYSTAL09 user's manual. University of Torino, Torino
46. Muscat J, Wander A, Harrison NM (2001) Chem Phys Lett 342:397–401
47. Bredow T, Gerson AR (2000) Phys Rev B 61:5194–5201
48. Zicovich-Wilson CM, Dovesi R (1998) J Phys Chem B 102:1411–1417
49. Calatayud M, Andres J, Beltran A (1999) Surf Sci 430:213–222
50. Zhang YF, Li JQ, Zhou LX (2001) Surf Sci 488:256–268
51. Zhang YF, Li JQ, Liu ZF (2004) J Phys Chem B 108:17143–17152
52. Zhang YF, Liu ZF (2004) J Phys Chem B 108:11435–11441
53. Zhang YF, Lin W, Li Y, Ding KN, Li JQ (2005) J Phys Chem B 109:19270–19277
54. Henrich VE, Cox PA (1994) The surface science of metal oxide. Cambridge University Press, Cambridge
55. Ágoston P, Albe K (2011) Surf Sci 605:714–722
56. Oviedo J, Gillan MJ (2000) Surf Sci 467:35–48
57. Bergermayer W, Tanaka I (2004) Appl Phys Lett 84:909–911
58. Rantala TT, Rantala TS, Lantto V (2000) Mater Sci Semi Pro 3:103–107
59. Mäki-Jaskari MA, Rantala TT (2001) Phys Rev B 64:075407-1-7
60. Batzill M, Katsiev K, Burst JM, Diebold U (2005) Phys Rev B 72:165414-1-20
61. Diebold U (2003) Surf Sci Rep 48:53–229
62. Oviedo J, Gillan MJ (2000) Surf Sci 463:93–101
63. Lide DR (2004) CRC handbook of chemistry and physics, 84th edn. CRC Press, Boca Raton FL
64. Epifani M, Prades JD, Comini E, Pellicer E, Avella M, Siciliano P, Faglia G, Cirera A, Scotti R, Morazzoni F, Morante JR (2008) J Phys Chem C 112:19540–19546
65. Sorescu DC, Yates JT (2002) J Phys Chem B 106:6184–6199
66. Bates SP, Kresse G, Gillan MJ (1997) Surf Sci 385:386–394
67. Charlton PBHG, Nicklin CL, Steadman P, Taylor JSG, Muryn CA, Harte SP, Mercer J, McGrath DNR, Turner TS, Thornton G (1997) Phys Rev Lett 78:495–498
68. Manassidis I, Goniakowski J, Kantorovich LN, Gillan MJ (1995) Surf Sci 339:258–271
69. Mäki-Jaskari MA, Rantala TT (2002) Phys Rev B 65:245428-1-6
70. Kawabe T, Tabata K, Suzuki E, Yamaguchi Y, Nagasawa Y (2001) J Phys Chem B 105:4239–4244
71. Radecka M, Zakrzewska K, Rekas M (1998) Sen Actuators B 47:194–204